Received: 13 July 2020 | Revised: 10 September 2020 | Accepted: 15 September 2020

DOI: 10.1002/xrs.3200

RESEARCH ARTICLE

X-RAY SPECTROMETRY WILEY

# Spectral X-ray computed micro tomography: 3-dimensional chemical imaging

**Jonathan Sittner[1,2] | Jose R. A. Godinho[1] | Axel D. Renno[1] | Veerle Cnudde[2,3] | Marijn Boone[4] | Thomas De Schryver[4] | Denis Van Loo[4] | Margarita Merkulova[2] | Antti Roine[5] | Jussi Liipo[5]**

[1]Helmholtz-Zentrum Dresden-Rossendorf, Helmholtz Institute Freiberg for Resource Technology, Freiberg, Germany

[2]PProGRess-UGCT, Geology Department, Ghent University, Ghent

[3]Department of Earth Sciences, Utrecht University, Utrecht, The Netherlands

[4]TESCAN XRE, Ghent, Belgium

[5]Outotec, Espoo, Finland

**Correspondence**
Jonathan Sittner, Helmholtz-Zentrum Dresden-Rossendorf, Helmholtz Institute Freiberg for Resource Technology, Chemnitzer Straße 40, 09599 Freiberg, Germany; PProGRess-UGCT, Geology Department, Ghent University, Krijgslaan 281/Building S8, B-9000, Ghent, Belgium.
Email: j.sittner@hzdr.de

**Funding information**
H2020 European Institute of Innovation and Technology

**Abstract**

We present a new approach to 3-dimensional chemical imaging based on X-ray computed micro tomography (CT), which enables the analysis of the internal elemental chemistry. The method uses a conventional laboratory-based CT scanner equipped with a semiconductor detector (CdTe). Based on the X-ray absorption spectra, elements in a sample can be distinguished by their specific K-edge energy. The capabilities and performance of this new approach are illustrated with different experiments, i.e. single pure element particle measurements, element differentiation in mixtures, and mineral differentiation in a natural rock sample. The results show that the method can distinguish elements with K-edges in the range of 20 to 160 keV, this corresponds to an element range from Ag to U. Furthermore, the spectral information allows a distinction between materials, which show little variation in contrast in the reconstructed CT image.

**KEYWORDS**

CT, mineral classification, photon-counting detector, spectral X-ray tomography, 3D imaging

## 1 | INTRODUCTION

3D characterization of materials is indispensable in many fields such as geology, materials science, or archeology [1–3]. Nevertheless, most methods are limited to 2D, which implies the loss of information. Techniques such as scanning electron microscopy (SEM), electron probe microanalysis (EPMA) or transmission electron microscopy (TEM) are commonly used in numerous application [4–11]. However, usually, the investigated features of a sample are 3-dimensional, thus a complete characterization would only be possible using a 3D technique.

The most common method for 3D investigations is X-ray computed micro tomography (CT) that has been used for many years in medical science, security, industrial inspection or geology [12–19]. In CT, X-ray absorption images (radiographs) from different angles of the sample are recorded during the scan, which are then computationally reconstructed as a voxelized 3D image. The intensity of each voxel depends on the attenuation coefficient of the sample at a particular point. This intensity can be calculated using the Lambert–Beer's law (Equation 1). Mathematically, it describes the attenuation of X-rays in the sample and therefore the transmitted intensity I [20]:

$$I = I_0 e^{-\int \mu(s) ds} \quad (1)$$

$I_0$ is the incident beam intensity and $\mu(s)$ is the linear attenuation coefficient along the X-ray path $s$ [20]. Here, $\mu$ determines the intensity value for each point in a sample. This value depends on parameters such as material density $\rho$, atomic number of elements $Z$, and X-ray energy $E$ [19–21]. Usually, the values of $\rho$ and $Z$ are unknown in a CT scan, making a material identification not possible. However, based on the attenuation contrast, that is, using the greyscale values in the reconstructed CT image, materials can be distinguished [2,22,23].

There have been different approaches to measure chemical data in 3D by combining CT with other analytical methods. One combination is 2D automated mineralogy techniques with CT. The focus of this method is the calibration of the CT data based on the 2D mineralogical information [24]. This combination is accurate and minerals can be classified though, it is time-consuming and needs two different analytical techniques. Another approach is X-ray absorption spectroscopy, which exploits changes in absorption edges (e.g., K-edges), sharp discontinuities in the absorption spectra. These sharp edges appear as an abrupt increase from weak to strong absorption in the spectrum and occur at energies of an electronic transition of an atom meaning that this method is element-specific [21]. Based on the position of the absorption edge in the spectrum, one can determine different elements in the sample. One 3D method making use of this phenomenon is dual-energy CT [25–28]. Dual-energy CT uses two sequential CT scans of a sample with different incident X-ray energies below and above K-edges of chemical elements in investigated materials, this allows a decomposition of materials containing different chemical elements [28–30]. Dual-energy CT is a useful addition to conventional CT and it is commonly used in medical and biological research [27,31]. Nevertheless, dual-energy CT is time-consuming and has its limitations with chemically complex samples that contain several elements with K-edges in the same measured energy range.

Besides conventional CT scanners with a polychromatic X-ray tube, there are different techniques for a 3D chemical imaging based on monochromatic synchrotron radiation, such as absorption-edge tomography, which uses X-rays tuned to specific absorption edges [32,33]. Additionally, 3D chemical information can also be complemented by X-ray absorption near-edge structure (XANES) and extended X-ray absorption fine structure (EXAFS), techniques sensitive to atomic environments of elements [34–39]. Alternately, there are synchrotron methods using X-ray fluorescence for 3D chemical imaging [40,41]. X-ray fluorescence in 3D has a higher sensitivity, at the cost of a slower scanning process, compared to the techniques mentioned above. All these methods using monochromatic synchrotron radiation provide high-resolution data and can even give additional information about oxidation states of elements or the coordination environment in the sample [39]. However, access to synchrotron facilities is much more limited than laboratory-based instruments.

Other 3D techniques use focused ion beams (FIB) instead of X-rays such as time-of-flight secondary ion mass spectrometry (FIB TOF-SIMS) and FIB-SEM [42–45]. FIB-based techniques provide high spatial and depth resolutions but are destructive due to the high intensity of the ion beam. Moreover, only small volumes can be scanned compared to other 3D techniques such as CT. Another destructive high-resolution method for a 3D material characterization is atom probe tomography where the sample is evaporated from a small tip and single atoms are detected [46].

As an alternative, a laboratory-based spectral X-ray micro-computed tomography (Sp-CT) is a promising approach as a 3D material identification method. Sp-CT uses a multi-pixel photon-counting detector (PCD) such as cadmium telluride (CdTe) or cadmium zinc telluride (CdZnTe) in combination with a conventional CT scanner to image a sample and detect its transmitted polychromatic X-ray spectrum [47–53]. Based on the position of elemental K-edges on recorded spectra chemically different particles can be identified inside a sample from a single CT scan [53]. This method based on 3D multi-pixel PCDs usually requires long measurement times. In this paper, we present Sp-CT with a 2D line detector, which decreases the acquisition time and allows performing fast scans without preparation of the sample.

In this paper, we describe the general principle of Sp-CT and the instrument including the photon-counting detector that we used. We present first results with a focus on 3D chemical characterization of geological samples and show the potential of this method in different fields of application.

## 2 | PRINCIPLE OF SPECTRAL-CT

Various processes occur in the interaction between X-rays and matter, for example, scattering, diffraction, absorption [21]. The linear attenuation (Equation (1)) is the main phenomenon that gives contrast differences in phases. The attenuation is caused by four major processes: incoherent or Compton scattering, coherent scattering, photoelectric effect, and pair production [20,21]. At low energies (50–100 keV) the photoelectric effect dominates the attenuation while at higher energies

(5–10 MeV) Compton scattering is dominant. Pair production is only relevant for very high energies [15,19,21]. For most laboratory CT setups, the main contribution to X-ray attenuation is the photoelectric effect, which can roughly be expressed by (Equation 2) [21].

$$\tau \cong constant \cdot \frac{Z^n}{E^{3.5}} \quad (2)$$

Here the exponent n varies between 4 and 5, meaning that the photoelectric effect increases steeply with the atomic number ($Z$). On the other hand, it decreases with increasing photon energy ($E$).

When the X-rays are attenuated by the sample, the spectrum of the primary X-rays emitted from the source is changed (Figure 1). Therefore, the spectrum of the X-rays transmitted through the sample contains information about the sample composition. Interpretation of the spectra resulted from an interaction of X-rays with a sample is the basis of Sp-CT. These spectra show different features such as abrupt changes in the transmission, which can be explained by absorption edges of certain elements. These sharp edges appear as transitions from weak to strong absorption, which is reversed in the transmission spectrum, that is, at an absorption edge the transmission decreases as a result of the increasing absorption. The absorption edges occur at energies of an electronic transition where the incoming X-ray photons correspond to the binding energy of the electron(s) in a particular electronic shell (K, L, M, etc.) of a specific atom. Thus, the technique is element specific, that is, one can determine different elements in the sample based on the energy position of the absorption edge [21].

The spectrum on which Sp-CT relies is detected by a PCD. To explain the difference between a conventional CT detector and a PCD the following section summarizes the operation of both detectors. A conventional CT detector consists of a scintillator crystal (e.g., CsI), which converts the incoming X-rays into visible light. Optical sensors such as CCD (charge-coupled device) or CMOS (complementary metal-oxide-semiconductor) detect and transform the visible light into an electronic signal. The signal is proportional to the total energy of all photons deposited within the readout time, thus information about individual photons is lost (energy integrating detector) [54]. This method of detection is also called indirect because X-rays are transformed into light before the detection. In contrast, a PCD uses a semiconductor crystal such as CdTe, CdZnTe, Se or Si that directly converts the incoming X-ray photon into an electric charge. Therefore, it is also called direct detection [55]. The detector consists of a single semiconductor crystal, two electrodes, and the readout electronics or application-specific integrated circuit (ASIC) (Figure 2). The cathode is a monolithic electrode and covers the whole semiconductor while the anode is pixelated and evenly distributed on the other side of the crystal [50]. A bias voltage is applied between the two electrodes. The pixelated anode is connected to the ASIC by bump bonds which usually consists of In or Pb/Sn [56]. For a larger detector area, multiple of these modules with separate semiconductor crystals can be placed next to each other. If an X-ray photon hits the detector it generates electron–hole-pairs in the semiconductor and the applied voltage causes a separation of these charge carriers to the contacts (Figure 2). The readout electronics further process and amplify the signal. They usually consist of a charge-sensitive

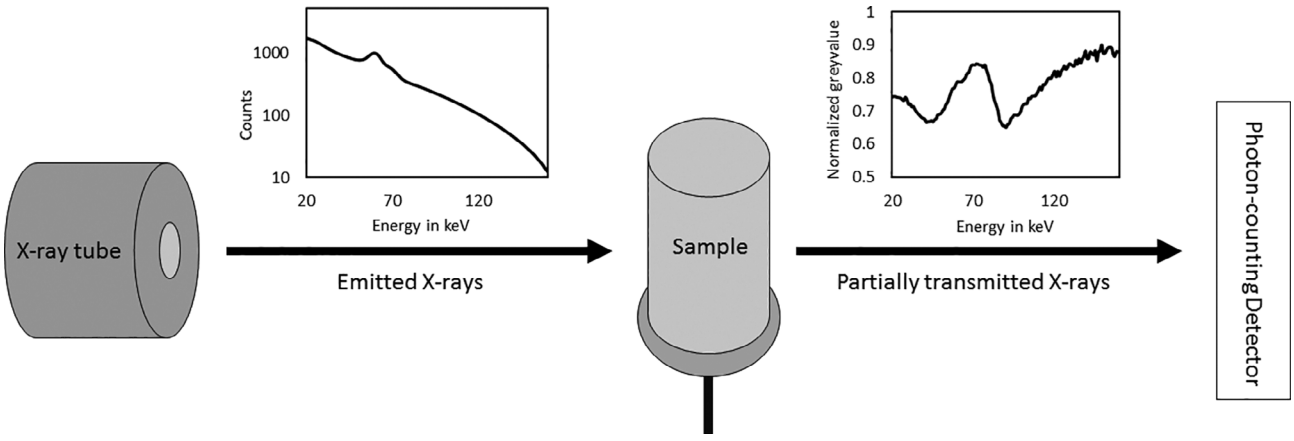


**FIGURE 1** Schematic principle of the Sp-CT with the initial spectrum of the X-rays as they are emitted by the Xray tube (left); the two visible peaks represent the tungsten K-α and K-β from the tungsten target in the Xray tube; The right spectrum shows the partially transmitted spectrum after the X-rays passed the sample (in this case a gold particle); the strong decrease in the transmission around 80 keV is the Au K-edge

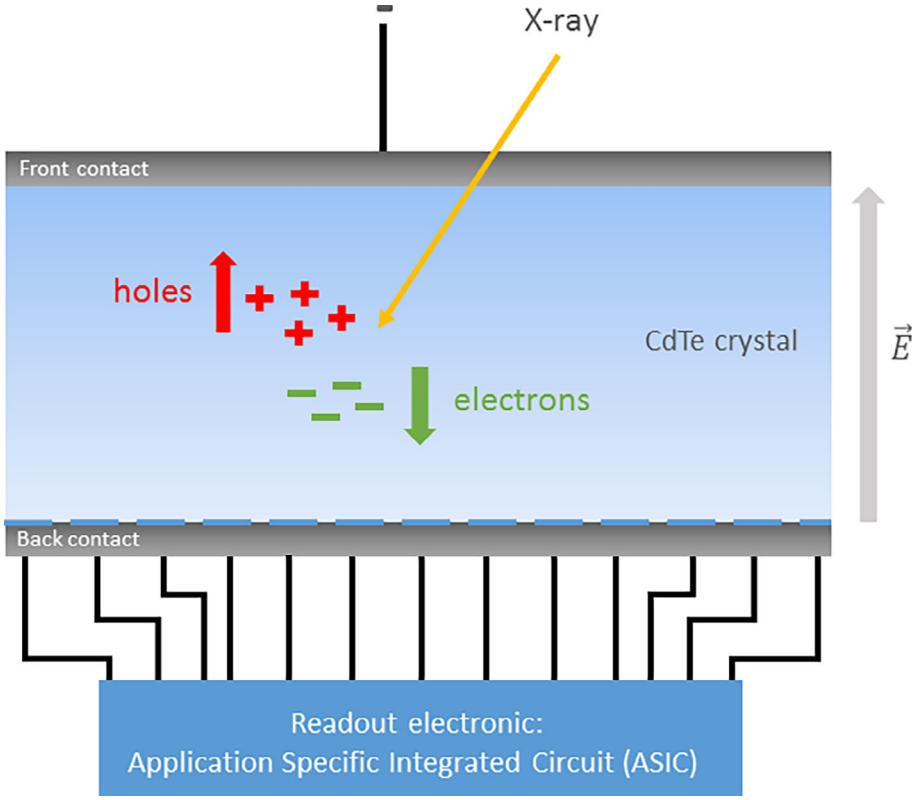


**FIGURE 2** Schematic operation of a photon-counting detector with a CdTe crystal; the X-rays produce electron–hole pairs, which are separated to the contacts due to the applied voltage in the CdTe crystal; the readout electronics further process and amplify the signal [Colour figure can be viewed at wileyonlinelibrary.com]

preamplifier, a pulse shaper, and multiple pairs of voltage pulse height comparator and digital counter [50]. The charge-sensitive preamplifier converts the incoming transient current into a charge. The pulse shaper not only shapes the signal but also amplifies the signal and reduces the noise produced by the preamplifier. The voltage pulse height comparator sets different energy thresholds to determine which pulse is processed further. It can be set individually for each pixel to compensate for different variations in the electronics [50]. In the end, the signal consists of a single voltage pulse, which is proportional to the energy of each individual detected X-ray photon.

Figure 3 shows the raw data from single radiographs, which were measured with a photon-counting line detector (TESCAN PolyDet). The *y*-direction of the radiographs represents the energy separated into different bins and the *x*-direction gives spatial information. In the flat field radiograph with no sample, numerous dark vertical lines are caused by the structure and the readout electronics of the detector. Another visible feature is the bright horizontal band, which extends across the entire radiograph. This represents the tungsten K-α fluorescence at 59.3 keV (NIST X-Ray Transition Energies Database; [57]). The W K-β fluorescence at 67.2 keV is also noticeable, but with less intensity (NIST X-Ray Transition Energies Database; [57]). The sample, in this case, a gold particle appears as a shadow in the image and after the normalization of both images, it is better visible. The normalization eliminates all features that do not originate from the sample. With this normalized radiograph, the spectrum of the sample can be extracted as seen in Figure 3. The strong decrease around 80 keV can be explained by the Au K-edge. In this case, the signal drops because the radiograph displays the transmission of the sample that decreases at the K-edge. At this particular energy, the sample is transmitting less x-rays due to the increased absorption at the Au K-edge.

To get a full scan with many radiographs from different angles, the sample needs to be rotated. The reconstruction of all radiographs measured with the line detector results in a two-dimensional image of the sample. The reconstruction contains 128 slices through the sample, one for each energy bin (see Section 3), showing not only the 2D spatial structure but also the spectral information (Figure 4). To scan a large 3D volume several 2D scans need to be stacked to get the 3-dimensional and spectral information.

In an ideal detector, each X-ray photon would interact and produce a pulse with a voltage that represents its energy. However, in the case of real detectors, there are physical and technical limitations that affect our spectrum. Some photons do not interact at all with the detector and pass through. Some scatter from the detector itself or the shielding and produce secondary effects that lower the initial signal [58]. The interaction physics between photons

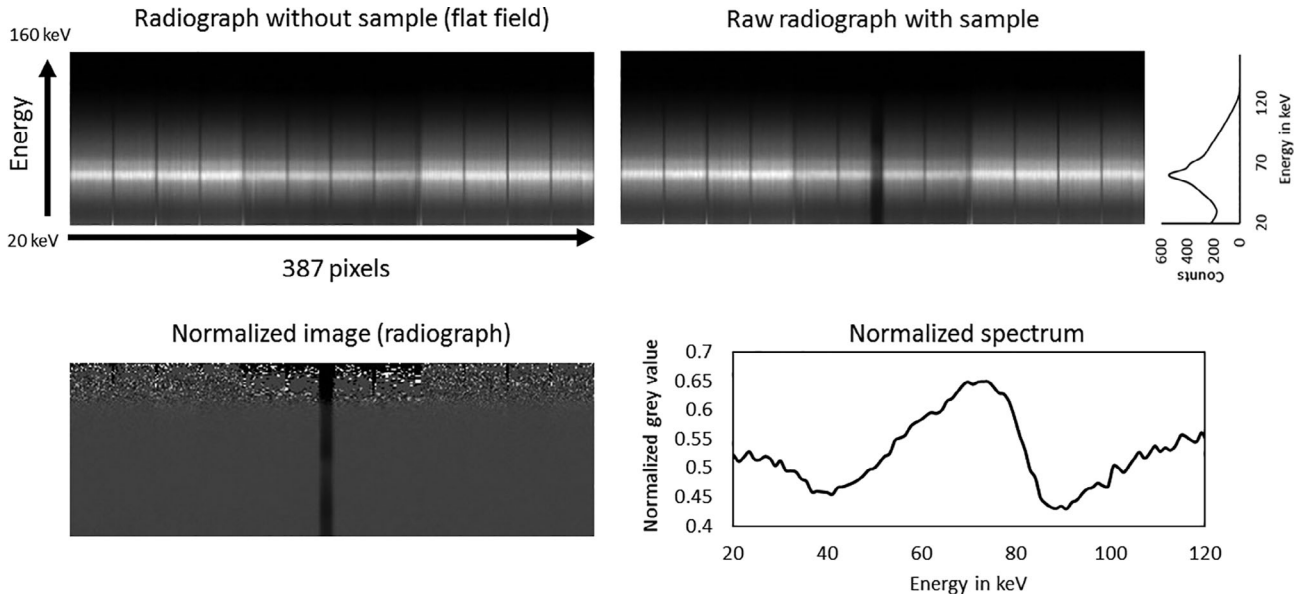


**FIGURE 3** Radiographs and spectrum measured with a photon-counting detector (PCD); top left: flat field without a sample, the vertical lines are caused by the readout electronics and the bright horizontal line represents the tungsten fluorescence from the X-ray tube; top right: radiograph with a sample visible as a shadow with the unnormalized spectrum on the right side; bottom left: normalized radiograph with the sample; bottom right: transmission spectrum of the sample (gold) with the K-edge around 80 keV

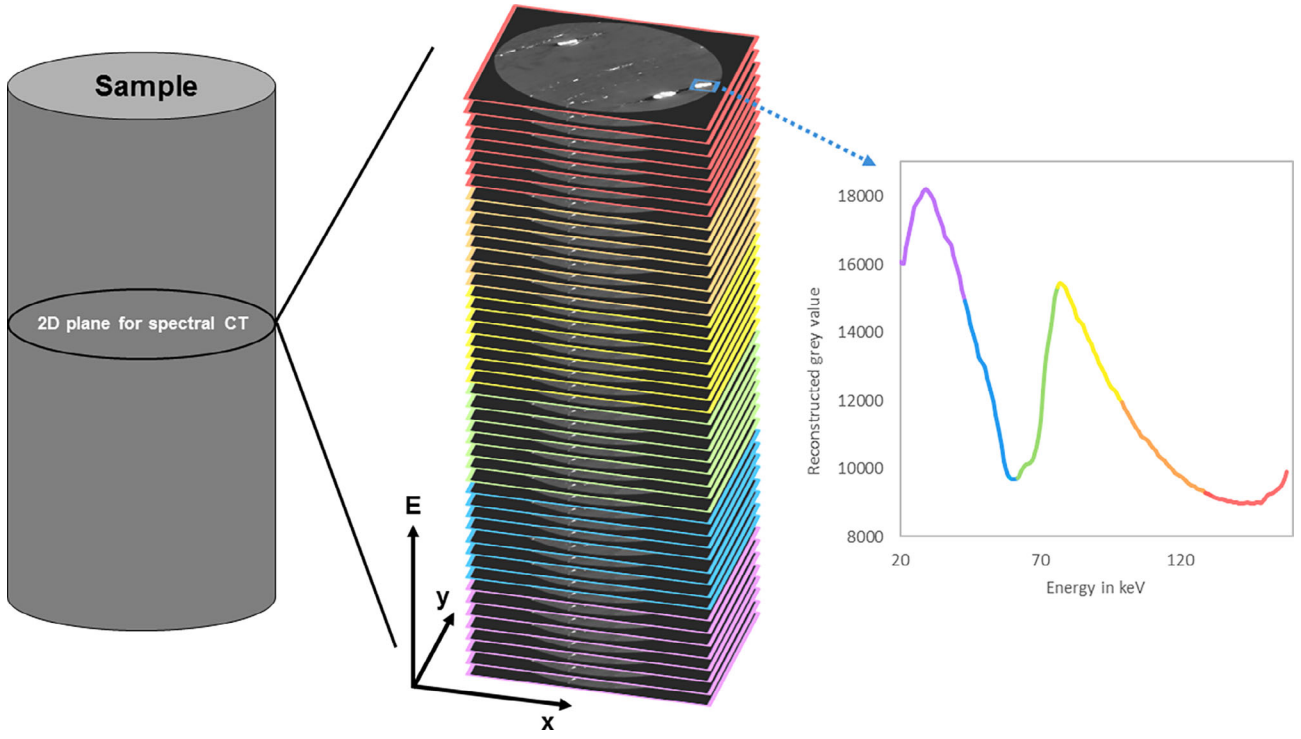


**FIGURE 4** Schematic principle of a full 360° scan of a sample with the line detector; the result is a stack of 128 images of the 2D slice of the sample for each energy bin; based on this image stack the spectrum can be extracted [Colour figure can be viewed at wileyonlinelibrary.com]

and the detector substrate also leads to an incomplete collection of photon energy, for example, charge sharing [50,53,59,60]. Finally, the electronic readout is distorted by, for example, electronic noise or pulse pile-up [21,49,61]. All these artifacts are common in different types of detectors and must be considered when interpreting the spectrum.

In a CdTe detector, Cd and Te are excited by the incident X-rays and produce specific X-rays. This affects all electron transitions (K, L) but the effect of K radiation is the strongest. Both Cd and Te produce K-α and K-β peaks in the measured spectral range. Table 1 shows their characteristic X-ray energies. When the primary X-rays hit the detector, they can produce secondary X-rays with the specific energies of Cd or Te. When this specific X-ray radiation leaves the detector without further interaction, then this portion of energy can no longer be detected and an escape peak with a precisely defined lower energy is formed (Figure 5) [21,62,63].

Pulse pile-up is another known possible artifact, which describes a case of two X-ray photons hitting the detector within the readout time. This results in the detection of just one event and an artificial signal that consists of two summed X-ray photons [21,49,61]. Therefore the counts are artificially increased at twice the energy, especially when E represents a peak value (Figure 5). Especially low to intermediate energies are dominated by electronic noise. However, the low energy threshold of the detector blocks out the dark noise and eliminates most of these artifacts. Charge sharing is a phenomenon that occurs in every pixelated detector and is reported for CdTe detectors too [64,65]. After an X-ray photon produced a charge cloud, this drifts towards the electrode and spreads laterally. Because the pixels are electrically separated by the bonds and not physically in the semiconductor crystal this charge cloud can spread over different neighboring pixels resulting in a sharing of induced current signals by multiple neighboring pixels. This reduces the measured signal in the specific pixel and contributes to a lower energy and lateral resolution [50,53,59,60].

**TABLE 1** Characteristic X-ray energies for Cd and Te, in keV (data from NIST X-Ray Transition Energies Database [57])

| | K-$\alpha_1$ | K-$\alpha_2$ | K-$\beta_1$ | K-$\beta_2$ |
|---|---|---|---|---|
| **Cd** | 23.17 | 22.98 | 26.09 | 26.06 |
| **Te** | 27.47 | 27.20 | 30.99 | 30.94 |

## 3 | METHODS

All scans presented in this study were performed with the TESCAN CoreTOM (Gent, Belgium and Freiberg, Germany). Apart from the standard imaging detector, the CoreTOM is equipped with an additional photon-counting line sensor, the TESCAN PolyDet, which can automatically slide in front of the standard detector. The PolyDet is a CdTe X-ray detector with a sensor width of 307 mm (Figure 6). The direct detection sensor has an energy range from 20 up to 160 keV and can discriminate up to 128 energy bins (Table 2). In particular, the K-edge of elements from Ag up to U can be detected with this detector.

Samples with different complexities were investigated: particles of pure metals (Pb, W, Au, and Sn), particle mixtures embedded in a low absorbing matrix and metal-bearing natural rocks (Table 3). The metal particles have been attached to a graphite stick using superglue for the Sp-CT measurements. For the mixtures, <400 μm quartz grains ($SiO_2$), were mixed as a low absorbing matrix mineral with the metal particles of interest, and the epoxy resin was used to solidify the mixture in a cylindrical plastic container with a diameter of 1 cm. The natural rock sample is a quarter of a drilling core of a gold-bearing rock from the Massawa orogenic gold deposit in Senegal. The sample contains a quartz vein

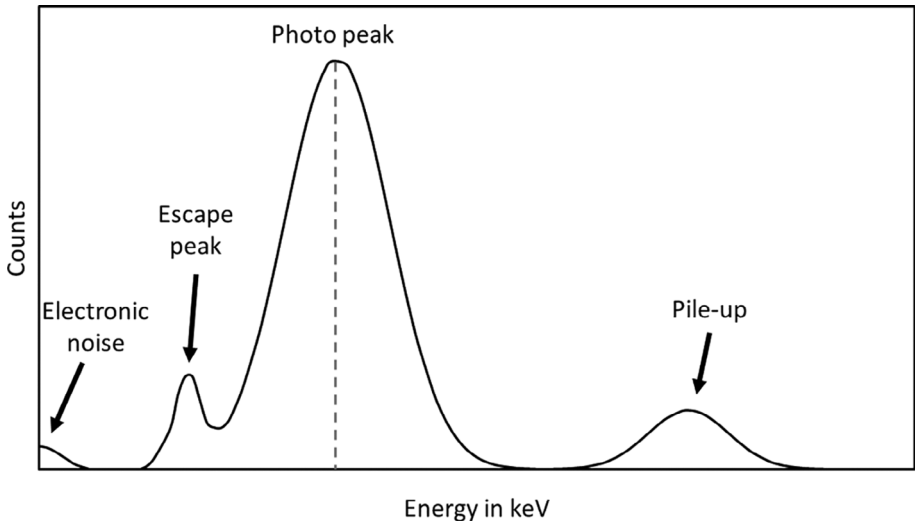


**FIGURE 5** Schematic illustration of the spectral response of a CdTe detector for a photo peak with important detector artifacts

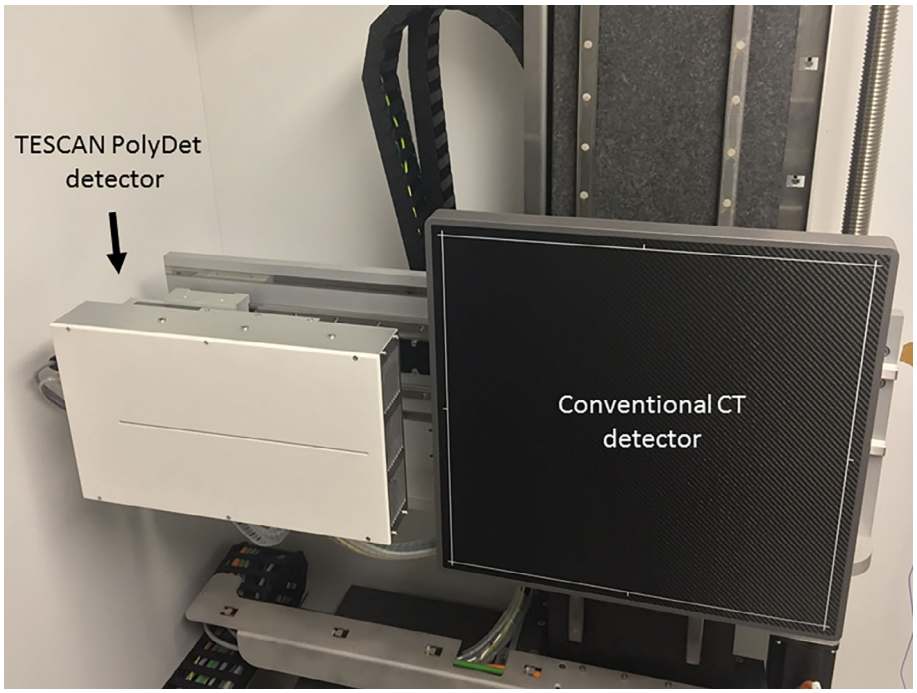


**FIGURE 6** The TESCAN PolyDet CdTe X-ray detector next to the 2,800 × 2,800 pixel detector; for a spectral measurement, the PolyDet can be moved into the beam path in front of the other detector [Colour figure can be viewed at wileyonlinelibrary.com]

**TABLE 2** General specifications of the TESCAN PolyDet

| Dimensions (W × H × D) | 398 × 236 × 76 mm |
|---|---|
| Radiation sensor | Cadmium telluride (CdTe) |
| Number of pixels | 384 |
| Sensor width | 307 mm |
| Energy range | 20–160 keV |
| Energy resolution | 9.1 keV FWHM at 96 keV |

**TABLE 3** Summary of investigated particle material with the formula, density, and particle size (data from Refs. [66, 67])

| Sample | Formula | Density | Size |
|---|---|---|---|
| Lead-particles | Pb | 11.34 g/cm$^3$ | 150 µm |
| Tungsten-particles | W | 19.25 g/cm$^3$ | 50–250 µm |
| Gold-particles | Au | 19.30 g/cm$^3$ | 250 µm |
| Tin-particles | Sn | 5.77 g/cm$^3$ | Ca. 500 µm |

with stibnite ($Sb_2S_3$) and other sulfides, and moderate pyrite ($FeS_2$)-arsenopyrite (FeAsS) selvages [68].

The measurement conditions were adapted to the respective samples and a detailed list is attached in Table A1 (Appendix). The voltage was usually set between 50 and 160 keV and the power between 10 and 100 W. Not only single radiographs but also 360° tomographic acquisition with 600 projection were performed using the line detector. Before each scan, a radiograph without a sample (flat field) was measured to normalize the images later. The duration of each Sp-CT scan was about 20 minutes. The radiographs were reconstructed using the spectral reconstruction module in Acquila reconstruction by Tescan (version 1.14) with a fan beam reconstruction, a ring filter, and a bad pixel correction (spot filter).

## 4 | RESULTS

In the results section, we first describe the polychromatic spectrum of the X-ray tube detected by the PCD. Furthermore, we present the results of the pure element particle measurements and the particle mixture embedded in a low absorbing matrix. In the end, we show the results of mineral differentiation in the rock sample.

### 4.1 | Polychromatic X-ray tube spectrum

Figure 7 shows the unfiltered polychromatic spectra of the X-ray tube recorded with a different maximum energy. The maximum energy of the tube in the individual scans is increasing starting at 40 keV and ending at 160 keV in steps of 20 keV with a power of 10 W. The spectra with a maximum energy above 80 keV show the characteristic tungsten K-α fluorescence at 59.3 keV caused by the tungsten target of the tube (NIST X-Ray Transition Energies Database; [57]). This normally distinct and sharp fluorescence peak is broadened by the PCDs energy response, which has an energy resolution of 9.1 keV

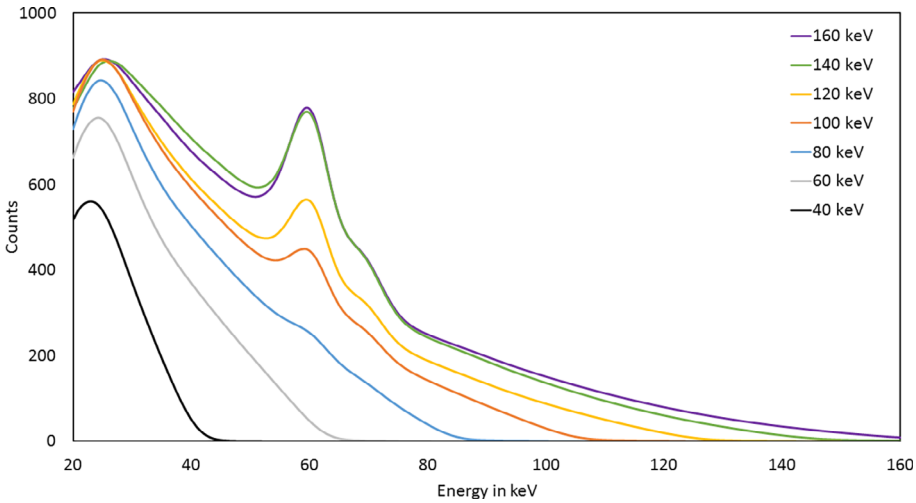


**FIGURE 7** Polychromatic spectrum of the X-ray tube measured with the TESCAN PolyDet with different maximum energies; the maximum energy of the tube is increasing starting at 40 keV and ending at 160 keV in steps of 20 keV with a power of 10 W and without a filter; the tungsten K-α fluorescence at 59.3 keV is visible in all scans with a maximum energy above 80 keV and K-β fluorescence at 67.2 keV appears as a small peak in all scans with a maximum energy above 100 keV (data from NIST X-Ray Transition Energies Database; [57]) [Colour figure can be viewed at wileyonlinelibrary.com]

FWHM at 96 keV. The less intense peak from W K-β fluorescence at 67.2 keV is only visible in the spectra with a maximum tube energy between 100 and 160 keV (NIST X-Ray Transition Energies Database; [57]). The W K-β peak appears on the right shoulder of the W K-α peak. Furthermore, the different spectra do not reach zero counts at their particular highest energy. There is a small shift towards higher energies in all spectra, which can be explained by several pulse pile-up events.

## 4.2 | Single particles

Different pure metal particles were investigated in this study to compare the measured and theoretical spectra and the position of the K-edges. Figure 8 shows two spectra measured on gold and lead particles, and the first derivative of the measured spectra and theoretical spectra corresponding to Au and Pb (data from the NIST Standard Reference Database 66, [69]). The first derivative is a good tool to compare the K-edge with its theoretical positions as the edge forms a distinct peak.

As is seen from the spectra the detector is capable of resolving the K-edges of particular elements in the spectral range. The measured spectra have differences compared to the theoretical spectra. One major difference is in the low energy range between 20 and ca. 60 keV, in which the measured spectrum shows lower intensities. Furthermore, there is a small peak around 60 keV in both spectra, which is also visible in the first derivative. This is probably an artifact from the tungsten K-α fluorescence. The K-edges of both elements are visible and their energy position corresponds to theoretical values. Widened-edge peaks on measured spectra are broader compared to theoretical spectra due to the energy resolution of the PCD as can be seen in Figure 7 for the tungsten fluorescence lines. The lead K-edge peak occurs at 90.3 keV, which is 2.3 keV higher than the theoretical position (88.0 keV; NIST X-Ray Transition Energies Database; [57]). A possible reason for this shift could be a detector artifact such as charge sharing. The gold K-edge peak occurs at 81.4 keV, which is 0.7 keV higher than a theoretical value (80.7 keV; NIST X-Ray Transition Energies Database; [57]). It fits well with the theory and it is in the range of the measurement uncertainty, which is relatively high compared to the lead value. This could be explained by the peak on the right shoulder in the first derivative, which makes it difficult to fit (Figure 8b).

Figure 8c and d shows the spectra measured on a pure tin particle and their first derivatives. This is a good example of a K-edge in the lower energy range, with the K-edge of tin at 29.2 keV (NIST X-Ray Transition Energies Database; [57]). The two spectra represent different measurement conditions one with 160 keV and 10 W (high energy) and the other with 50 keV and 10 W (low energy). The spectra differ in the calculated attenuation, with the low energy measurement showing a higher attenuation. The signal at the tin K-edge is also different and the low energy measurement shows a steeper slope. The spectrum of the low energy measurement reaches zero at around 75 keV. However, the maximum energy of the tube is 50 keV. This effect cannot be explained by primary X-ray photons from the tube because it does not emit any X-ray photons with more than 50 keV. It is due to detector artifacts and primarily caused by several pile-up events in the flat field. Figure 8f shows the first derivative of the two spectra to compare the signal at the K-edge. The low energy measurement shows a higher peak at the K-edge and is better optimized for the Sn particle.

The single particle measurements show deviations from theoretical values. Nevertheless, the position of K-edges is determined within analytical feasibility. The

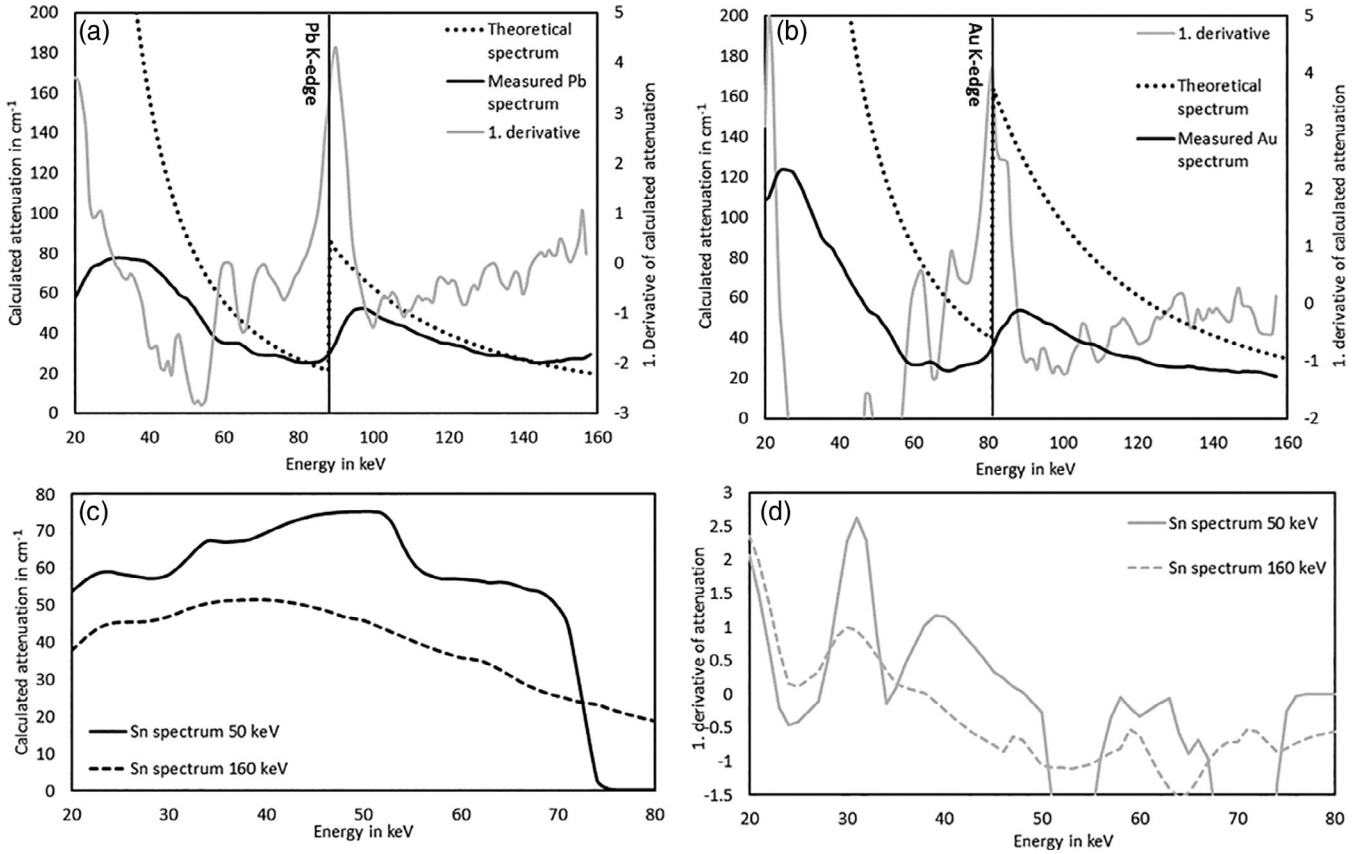


**FIGURE 8** Measured spectra of pure lead, gold, and tin particles, first derivatives of the measured spectra and theoretical spectra of Pb and Au (data from the NIST Standard Reference Database 66, [69] and NIST X-Ray Transition Energies Database; [57]): (a) theoretical and measured spectra of a lead particle with the first derivative of the measured spectrum and the theoretical position of the Pb K-edge (88.0 keV); (b) theoretical and measured spectra of a gold particle with the first derivative of the measured spectrum and the theoretical position of the Au K-edge (80.7 keV); (c) spectrum of a tin particle measured with 160 keV and 10 W and with 50 keV and 10 W (without filter); (d) the first derivative of the Sn-spectrum measured with 160 keV and 10 W and with 50 keV and 10 W (without filter)

demonstrated method is conclusive regarding the identification of pure elemental particles based on the determination of elemental K-edges in the spectral region. However, more detector and processing improvements are necessary to remove spectral artifacts for achieving a better quality of measured spectra.

## 4.3 | Particle mixtures

A more complex sample is used for material identification in the presence of different elements. The sample consists of gold, lead, and tungsten particles which were mixed with quartz as a matrix material to simulate a chemically complex rock (Table 3). This sample serves as a comparison to the single particle measurements, whereby the position of the respective edges should be compared. Furthermore, the material identification of both a conventional CT image and a Sp-CT image are compared.

Figure 9a and b shows the reconstructed CT image of the mixture in comparison to the reconstructed and summed Sp-CT image (sum of all 128 energy bins). A major difference between the two images is spatial resolution. The voxel size of the scans differs from 11.5 μm of the CT scan to 52.5 μm of the Sp-CT scan. The number of pixels of the PCD limits the resolution of the Sp-CT image and the individual particles appear blurry compared to the conventional CT image.

The grey value histogram is typically used for a material identification based on the reconstructed CT image (Figure 9c). Individual peaks in the histogram are assigned to the respective materials. In a perfect case, each material would have its peak in the histogram on which the reconstructed image can be segmented. However, the histogram in Figure 9 shows no or small peaks. The double peak at a grey value of around 5,000 represents the air or resin in the sample and the matrix mineral, in this case, quartz. Even though the particles in the sample have a different elemental composition and

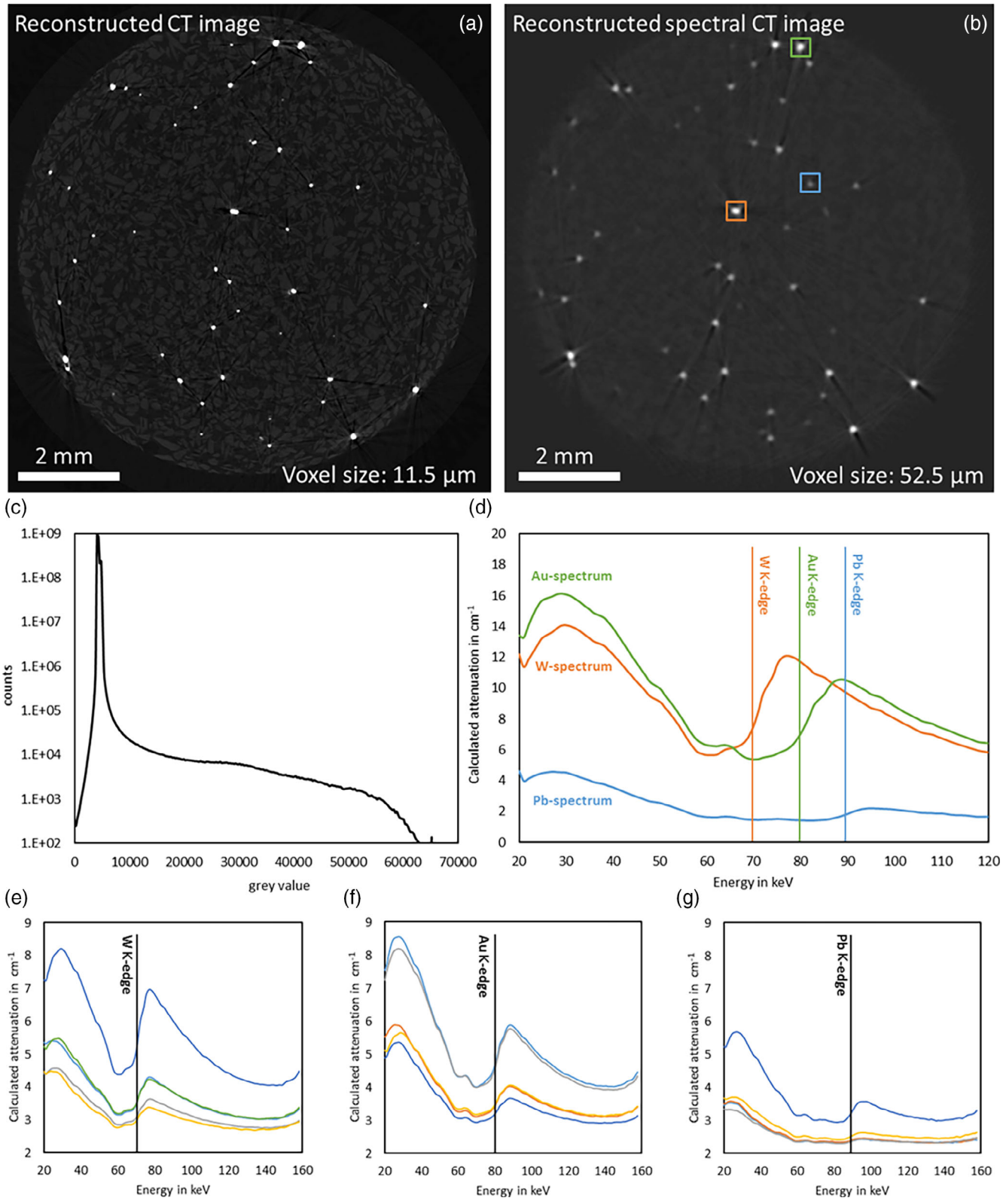


**FIGURE 9** Reconstructed CT images, energy spectra and gray value histogram: a: reconstructed CT image (160 keV, 15 W, no filter); b: reconstructed summed Sp-CT image (160 keV, 20 W, no filter); c: grey value of the CT scan image as a function of number of counts (grey value histogram), y-axis in logarithmic scale; d: energy spectra of the different particles with the theoretical K-edge positions of Au, Pb and W; e: five W spectra with the theoretical K-edge position; f: five Au spectra with the theoretical K-edge positions; g: five Pb spectra with the theoretical K-edge positions (NIST X-Ray Transition Energies Database; [57]) [Colour figure can be viewed at wileyonlinelibrary.com]

densities, the histogram shows no peaks on which the particles can be separated. This can be explained by the total number of voxels, whereby the individual particles represent only a small amount in contrast to the matrix and the air. Therefore, a material identification based on a conventional CT scan is very difficult in that case.

With the Sp-CT scan, the spectra of the individual particles can be analyzed to identify the particle chemistry. Figure 9d shows three different spectra from particles, which are marked in the reconstructed Sp-CT image (Figure 9b). Even though the grey values of the marked particles in the Sp-CT image are the same, the particle spectra show different characteristics and different positions of K-edges in the measured spectral range. The Pb-spectrum shows the lowest signal with the K-edge energy position comparable with the theory (NIST X-Ray Transition Energies Database; [57]). The small particle size results in an averaging with the surrounding pixels, which can explain the low signal of the Pb particle (partial volume effect; [18]). The spectra of gold and tungsten show higher intensities and well visible K-edges. Energy positions of both K-edges are close to the theoretical values and it is easy to differentiate the Au and Pb particles based on their spectra. (NIST X-Ray Transition Energies Database; [57]).

Figure 9e, f, and g shows several spectra for each particle type in the sample. The intensities in all particle types vary but the K-edge positions of the specific elements are comparable with the theory (NIST X-Ray Transition Energies Database; [57]). Especially the energy range from 20 to 60 keV shows variations in the calculated attenuation. This could be explained by artifacts such as escape peaks. As mentioned above, since the particles have different sizes an averaging of the particle with the matrix pixels can cause a variation in the spectral intensity. Furthermore, the position of the particle in the sample and surrounding particles can also influence the overall intensity but not on the K-edge energy position.

Based on the different K-edge positions all particles in the solid mixture can be identified because Sp-CT scan gives information about the elements present in the individual particles. In combination with the conventional CT scan, additional high-resolution particle information is accessible.

### 4.4 | Rock samples

For a real case scenario, a gold-bearing rock from the Massawa deposit in Senegal was measured using CT and Sp-CT to find gold grains in the sample. First, a conventional CT scan was performed to identify areas of high attenuating minerals, second, Sp-CT was used to further chemically differentiate minerals. Figure 10a, b, and c shows the two reconstructed Sp-CT scans from different areas of the sample and the energy spectra of different minerals. The spectra show different absorption edges, two of which correspond to the theoretical position of the Au K-edge. The Au-spectra show the highest calculated attenuation of all measured spectra. They also display a small peak at around 40 keV, which is not visible in the other spectra. This could be an artifact, as it shows no characteristic of a K-edge. Another spectrum includes K-edge, the position of which corresponds to the theoretical K-edge of Pb. Notably, the Pb spectrum shows a lower calculated attenuation than Au spectra. Three spectra of less attenuating mineral grains, possibly represented by sulfide minerals or silicates, show the absence of an absorption edge, as they contain no element with a K-edge in the measured spectral range. The spectra of Au and Pb measured in the natural rock are similar to the spectra measured on single particles of pure elements (Figure 8a and b) but their calculated attenuation is lower. One reason for that is the use of a 1 mm Cu filter for the rock samples scans. It decreases the intensity of the X-rays especially at low energies but does not affect the K-edge position. Another reason for the lower calculated attenuation could be a possible capturing of the surrounding matrix or the amount of Au or Pb in a mineral. These factors, which did not significantly limit measurements of single particles of pure elements, can lead to a change in the calculated attenuation of mineral grains in a natural rock. However, the energy positions of K-edges cannot be affected by these factors and minerals can be chemically differentiated based on the K-edge positions in corresponding spectra. A more accurate identification of the mineral composition would only be possible by using additional techniques. Nonetheless, based on the Sp-CT scanning gold-bearing minerals contained in an ore sample can be distinguished without any sample preparation. This approach can be used as a first analytical step to define regions of interest, and high-resolution 2D methods can be used afterwards to determine a more precise chemical composition of minerals.

## 5 | OUTLOOK

Sp-CT is a relatively new method for 3-dimensional material identification and offers a promising new potential. We have shown that it is possible to distinguish between K-edges in the respective spectral range used and to identify materials in mixed samples using the edge position without any sample preparation. Sp-CT opens exciting new possibilities for elemental and mineral analysis.

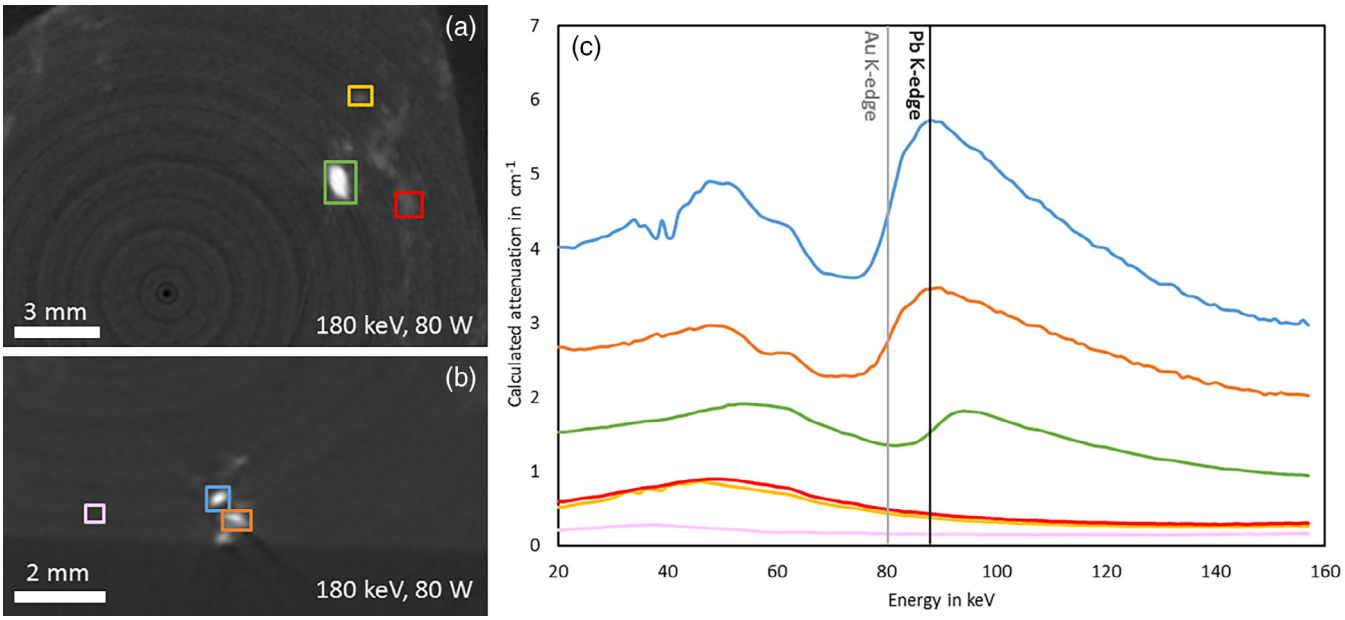


**FIGURE 10** (a) and (b) Reconstructed Sp-CT images (180 keV, 80 W) of two different planes in the natural rock sample (c) energy spectra of different particles indicated in (a and b) with the corresponding colors and theoretical positions of the Pb and the Au K-edges; note that the three spectra (red, yellow, and pink) possibly represented by sulfide minerals or silicates show no K-edge in the spectral range (NIST X-Ray Transition Energies Database; [57]) [Colour figure can be viewed at wileyonlinelibrary.com]

With this technique, the 3-dimensional properties of particles can be measured and used for example in process mineralogy simulations. At the moment such simulations use 2D or bulk particle properties. With a combination of CT with Sp-CT, the 3D properties and chemical information of different particles can be extracted for an improved simulation. The analyzed volume compared to 2D techniques is also larger and therefore more representative. This is a major improvement to current simulations. Moreover, Sp-CT could potentially be used as an alternative technique for a regular characterization of ores and processed ores since more representative volumes can be analyzed. Sp-CT can also serve as a primary analytical method on which subsequent higher resolution methods like SEM or EPMA can be based. A next step in the development is the establishment of an automated way of material identification using the spectrum and the K-edge position. Furthermore, improvements on the detector and the spectrum are necessary to optimize the signal and to remove artifacts.

## ACKNOWLEDGEMENTS

This research is part of the upscaling project “Resource Characterization: from 2D to 3D microscopy” and has received funding from the European Institute of Innovation and Technology (EIT), a body of the European Union, under the Horizon 2020, the EU Framework Program for Research and Innovation. Open access funding enabled and organized by Projekt DEAL.

## ORCID

*Jonathan Sittner* https://orcid.org/0000-0001-6733-8602

## REFERENCES

[1] T. Freeth, Y. Bitsakis, X. Moussas, J. H. Seiradakis, A. Tselikas, H. Mangou, M. Zafeiropoulou, R. Hadland, D. Bate, A. Ramsey, M. Allen, A. Crawley, P. Hockley, T. Malzbender, D. Gelb, W. Ambrisco, M. G. Edmunds, *Nature* **2006**, *444*, 587–91.

[2] P. Sylvester, V. Cnudde, J. Dewanckele, W. de Boever, L. Brabant, T. de Kock Eds., 3D characterization of grain size distributions in sandstone by means of X-ray computed tomography. in *Quantitative mineralogy and microanalysis of sediments and sedimentary rocks*. Quebec City: Mineralogical Association of Canada (MAC), **2012**, pp. 99–113.*Short Course Series Quant. Mineral. Microanal. sediments Sediment. rocks* 42, 99

[3] E. Maire, P. J. Withers, *Int. Mater. Rev.* **2014**, *59*, 1–43.

[4] M. Almgren, K. Edwards, G. Karlsson, *Colloids Surf. A Physicochem. Eng. Asp.* **2000**, *174*, 3–21.

[5] D. Mori, K. Yamada, *J. Adv. Conc. Technol.* **2007**, *5*, 285–98.

[6] K. W. Urban, *Science* **2008**, *80*, 321–506.

[7] S. D. Findlay, N. Shibata, H. Sawada, E. Okunishi, Y. Kondo, T. Yamamoto, Y. Ikuhara, *Appl. Phys. Lett.* **2009**, *95*, 10.

[8] R. Rinaldi, X. Llovet, *Microsc. Microanal.* **2015**, *21*, 1053–69.

[9] K. Bachmann, M. Frenzel, J. Krause, J. Gutzmer, *Microsc. Microanal.* **2017**, *23*, 527–37.

[10] K. Bachmann, I. Osbahr, R. Tolosana-Delgado, D. Chetty, J. Gutzmer, *Can. Mineral.* **2018**, *56*, 723–43.

[11] J. Liipo, M. Hicks, V. P. Takalo, A. Remes, M. Talikka, S. Khizanishvili, M. Natsvlishvili, *J. South African Inst. Min. Metall.* **2019**, *119*, 333.

[12] J. Gawler, M. D. Sanders, J. W. D. Bull, G. du Boulay, J. Marshall, *Br. J. Ophthalmol.* **1974**, *58*, 571–87.
[13] G. C. Conroy, M. W. Vannier, *Nature* **1987**, *329*, 625–7.
[14] X. Boespflug, B. F. N. Long, S. Occhietti, *Mar. Geol.* **1995**, *122*, 281–301.
[15] R. A. Ketcham, W. D. Carlson, *Comput. Geosci.* **2001**, *27*, 381–400.
[16] K. Steppe, V. Cnudde, C. Girard, R. Lemeur, J.-P. Cnudde, P. Jacobs, *J. Struct. Biol.* **2004**, *148*, 11–21.
[17] M. A. Boone, P. Nielsen, T. De Kock, M. N. Boone, M. Quaghebeur, V. Cnudde, *Environ. Sci. Technol.* **2014**, *48*, 674–80.
[18] J. R. A. Godinho, M. Kern, A. D. Renno, J. Gutzmer, *Miner. Eng.* **2019**, *144*, 106016.
[19] V. Cnudde, M. N. Boone, *Earth-Sci. Rev.* **2013**, *123*, 1–17.
[20] F. H. Attix, *Int. J. Radiat. Appl. Instrum. Part A. Appl. Radiat. Isot* **1987**, *38*, 163.
[21] G. F. Knoll, *Radiation detection and measurement*. New York: Wiley, **2000**.
[22] S. Ikeda, T. Nakano, A. Tsuchiyama, K. Uesugi, Y. Suzuki, K. Nakamura, Y. Nakashima, H. Yoshida, *Am. Mineral.* **2004**, *89*, 1304–13.
[23] R. Meftah, J. Van Stappen, S. Berger, G. Jacqus, J. Y. Laluet, P. H. Guering, L. Van Hoorebeke, V. Cnudde, *Materials (Basel)* **2019**, *12*, 1944–1957.
[24] F. Reyes, Q. Lin, O. Udoudo, C. Dodds, P. D. Lee, S. J. Neethling, *Miner. Eng.* **2017**, *110*, 122–30.
[25] R. E. Alvarez, A. Rtacovski, *Phys. Med. Biol.* **1976**, *21*, 733–44.
[26] T. G. Flohr, C. H. McCollough, H. Bruder, M. Petersilka, K. Gruber, C. Süß, M. Grasruck, K. Stierstorfer, B. Krauss, R. Raupach, A. N. Primak, A. Küttner, S. Achenbach, C. Becker, A. Kopp, B. M. Ohnesorge, *Eur. Radiol.* **2006**, *16*, 256–68.
[27] A. Graser, T. R. C. Johnson, H. Chandarana, M. Macari, *Eur. Radiol.* **2009**, *19*, 13–23.
[28] G. J. Pelgrim, R. W. van Hamersvelt, M. J. Willemink, B. T. Schmidt, T. Flohr, A. Schilham, J. Milles, M. Oudkerk, T. Leiner, R. Vliegenthart, *Eur. Radiol.* **2017**, *27*, 3904–12.
[29] C. E. Cann, G. Gamsu, F. A. Birnberg, W. R. Webb, *Radiology* **1982**, *145*, 493–6.
[30] H. Chandarana, A. J. Megibow, B. A. Cohen, R. Srinivasan, D. Kim, C. Leidecker, M. Macari, *AJR. Am. J. Roentgenol.* **2011**, *196*, W693–700.
[31] T. R. C. Johnson, B. Krauß, M. Sedlmair, M. Grasruck, H. Bruder, D. Morhard, C. Fink, S. Weckbach, M. Lenhard, B. Schmidt, T. Flohr, M. F. Reiser, C. R. Becker, *Eur. Radiol.* **2007**, *17*, 1510–7.
[32] P. Bleuet, P. Gergaud, L. Lemelle, P. Bleuet, R. Tucoulou, P. Cloetens, J. Susini, G. Delette, A. Simionovici, *TrAC Trends Anal. Chem.* **2010**, *29*, 518–27.
[33] S. R. Stock, *Int. Mater. Rev.* **2008**, *53*, 129–81.
[34] D. E. Sayers, E. A. Stern, F. W. Lytle, *Phys. Rev. Lett.* **1971**, *27*, 1204–7.
[35] P. Eisenberger, B. M. Kincaid, *Science* **1978**, *200*, 1441–7.
[36] G. R. Shulman, Y. Yafet, P. Eisenberger, W. E. Blumberg, *Proc. Natl. Acad. Sci.* **1976**, *73*, 1384–8.
[37] H. A. O. Hill, P. J. Sadler, and A. J. ThomsonJ. E. Penner-Hahn, Structural characterization of the Mn site in the photosynthetic oxygen-evolving complex, SpringerBerlin, Heidelberg, **1998**, 1–36.
[38] K. Sauer, J. Yano, V. K. Yachandra, *Coord. Chem. Rev.* **2008**, *252*, 318–35.
[39] X.-r. a. spectroscopy, J. Yano, V. K. Yachandra, *Photosynth. Res.* **2009**, *102*, 241.
[40] B. Kanngießer, W. Malzer, I. Reiche, *Nucl. Instrum. Methods Phys. Res. Sect. B Beam Interact. Mater. Atoms* **2003**, *211*, 259.
[41] S. Cagno, G. Nuyts, S. Bugani, K. De Vis, O. Schalm, J. Caen, L. Helfen, M. Cotte, P. Reischig, K. Janssens, *J. Anal. Atom. Spectrom.* **2011**, *26*, 2442.
[42] H. Nygren, B. Hagenhoff, P. Malmberg, M. Nilsson, K. Richter, *Microsc. Res. Tech.* **2007**, *70*, 969–74.
[43] M. A. Robinson, D. J. Graham, D. G. Castner, *Anal. Chem.* **2012**, *84*, 4880–5.
[44] J. S. Fletcher, N. P. Lockyer, J. C. Vickerman, *Mass Spectrom. Rev.* **2011**, *30*, 142–74.
[45] J. Brison, M. A. Robinson, D. S. W. Benoit, S. Muramoto, P. S. Stayton, D. G. Castner, *Anal. Chem.* **2013**, *85*, 10869–77.
[46] T. F. Kelly, M. K. Miller, *Rev. Sci. Instrum.* **2007**, *78*, 031101.
[47] M. Campbell, E. H. M. Heijne, G. Meddeler, E. Pernigotti, W. Snoeys, *IEEE Trans. Nucl. Sci.* **1998**, *45*, 751–3.
[48] E. C. Frey, K. Taguchi, M. Kapusta, J. Xu, T. Orskaug, I. Ninive, D. Wagenaar, B. Patt, B. M. W. Tsui, *Phys. Med. Imaging* **2007**, *6510*, 65101.
[49] K. Taguchi, M. Zhang, E. C. Frey, X. Wang, J. S. Iwanczyk, E. Nygard, N. E. Hartsough, B. M. W. Tsui, W. C. Barber, *Med. Phys.* **2011**, *38*, 1089–102.
[50] L. Ren, B. Zheng, H. Liu Eds., *J. Xray. Sci. Technol.* **2018**, *26*, 1.
[51] C. K. Egan, S. D. M. Jacques, M. D. Wilson, M. C. Veale, P. Seller, A. M. Beale, R. A. D. Pattrick, P. J. Withers, R. J. Cernik, *Sci. Rep.* **2015**, *5*, 15979
[52] I. Kumpova, M. Vopalensky, T. Fila, D. Kytyr, D. Vavrik, M. Pichotka, J. Jakubek, Z. Kersner, J. Klon, S. Seitl, J. Sobek, *IEEE Trans. Nucl. Sci.* **2018**, *65*, 2870–6.
[53] X. Wang, D. Meier, S. Mikkelsen, G. E. Maehlum, D. J. Wagenaar, B. M. W. Tsui, B. E. Patt, E. C. Frey, *Phys. Med. Biol.* **2011**, *56*, 2791–816.
[54] W. Zhou, J. I. Lane, M. L. Carlson, M. R. Bruesewitz, R. J. Witte, K. K. Koeller, L. J. Eckel, R. E. Carter, C. H. McCollough, S. Leng, *Am. J. Neuroradiol.* **2018**, *39*, 1733–8.
[55] G. Prekas, H. Sabet, H. Bhandari, G. Derderian, F. Robertson, H. Kudrolli, C. Stapels, J. Christian, S. Kleinfelder, S. Cool, L. D'Aries, V. Nagarkar, *IEEE Nucl. Sci. Symp. Conf. Rec.* **2012**, 1487–1493.
[56] T. Schulman, *Si, CdTe and CdZnTe radiation detectors for imaging applications*. Helsinki: Helsingin yliopisto; **2006**.
[57] R. D. Deslattes, E. G. Kassler, P. Indelicato, L. De Billy, E. Lindroth, J. Anton, *Rev. Mod. Phys.* **2003**, *75*, 35–99.
[58] R. Redus, J. Pantazis, T. Pantazis, A. Huber, B. Cross, *Nucl. Sci. IEEE Trans.* **2009**, *56*, 2524–32.
[59] K. Iniewski, H. Chen, G. Bindley, I. Kuvvetli, C. Budtz-Jørgensen, *IEEE Nucl. Sci. Symp. Conf. Rec.* **2007**, 4608–4611.
[60] M. C. Veale, S. J. Bell, L. L. Jones, P. Seller, M. D. Wilson, C. Allwork, D. Kitou, P. J. Sellin, P. Veeramani, R. C. Cernik, *IEEE Trans. Nucl. Sci.* **2011**, *58*, 2357–62.
[61] S. Usman, A. Patil, *Nucl. Eng. Technol.* **2018**, *50*, 1006–16.
[62] R. Tanaka, K. Yuge, J. Kawai, H. Alawadhi, *X-Ray Spectrom.* **2017**, *46*, 5–11.
[63] E. S. Dreier, J. Kehres, M. Khalil, M. Busi, Y. Gu, R. K. Feidenhans'l, U. L. Olsen, *Opt. Eng.* **2018**, *57*, 054117.

[64] M. Maiorino, G. Pellegrini, G. Blanchot, M. Chmeissani, J. Garcia, R. Martinez, M. Lozano, C. Puigdengoles, M. Ullan, *Nucl. Instrum. Methods Phys. Res. Sect. A Accel. Spectrom. Detect. Assoc. Equip.* **2006**, *563*, 177.
[65] D. Pennicard, C. Fleta, R. Bates, V. O'Shea, C. Parkes, G. Pellegrini, M. Lozano, J. Marchal, N. Tartoni, *Nucl. Instrum. Methods Phys. Res. Sect. A Accel. Spectrom. Detect. Assoc. Equip.* **2009**, *604*, 412.
[66] J. A. Dean, *Lange's Handbook of Chemistry*. 15. New York: McGraw-Hill, Inc; **1996**.
[67] D. R. Lide, *CRC Handbook of Chemistry and Physics*. 84 Boca Raton: CRC Press; **2003**.
[68] P. J. Treloar, D. M. Lawrence, D. Senghor, A. Boyce, P. Harbidge, *Geol. Soc. Lond. Spec. Publ.* **2015**, *393*, 135.
[69] C. T. Chantler, *J. Synchrotron. Radiat.* **2001**, *8*, 1124.

**How to cite this article:** Sittner J, Godinho JRA, Renno AD, et al. Spectral X-ray computed micro tomography: 3-dimensional chemical imaging. *X-Ray Spectrom*. 2021;50:92–105. https://doi.org/10.1002/xrs.3200

## APPENDIX A.

**TABLE A1** Scan settings for each scan

| Sample | Tube voltage | Tube power | Voxel size | Filter |
|---|---|---|---|---|
| Lead particle | 160 keV | 10 W | 13.1 μm | No filter |
| Gold particle | 160 keV | 10 W | 11.6 μm | No filter |
| Tin particle high keV | 160 keV | 10 W | 23.9 μm | No filter |
| Tin particle low keV | 50 keV | 10 W | 24.7 μm | No filter |
| Au-W-Pb mixture CT | 160 keV | 15 W | 11.5 μm | No filter |
| Au-W-Pb mixture Sp-CT | 160 keV | 20 W | 52.5 μm | No filter |
| Gold-bearing ore scan a | 180 keV | 80 W | 81.5 μm | 1 mm cu |
| Gold-bearing ore scan b | 180 keV | 80 W | 81.5 μm | 1 mm cu |